Check for updates

ADVANCED FUNCTIONAL MATERIALS
www.afm-journal.de

Enhancement of Phase Stability and Thermoelectric Performance of Meta-Stable $AgSbTe_2$ by Thermal Cycling Process

Jin Hee Kim, Jae Hyun Yun, Seunghun Cha, Seokyeong Byeon, Junyoung Park, Hyungyu Jin, Sujin Kim, Sung-Jin Kim, JongHo Park, Jeongin Jang, SuDong Park, and Jong-Soo Rhyee**

Thermoelectric materials are crucial components in thermoelectric devices employed for environmentally friendly solid-state cooling and waste heat recovery, demanding not only high performance but also superior thermal or phase stability. The high-performance thermoelectric material $AgSbTe_2$ encounters challenges when utilized in thermoelectric modules due to the precipitation of Ag_2Te, resulting in both thermally unstable characteristics and diminished performance. In this study, a thermal cycling process is employed to enhance the thermal stability and thermoelectric performance of $AgSbTe_2$. Through thermal cycling, secondary phases of $AgSbTe_2$ are made uniform, and the undesired Ag_2Te is substituted with Sb_2Te_3 using an optimized thermal cycling process. As a result, the thermal stability of $AgSbTe_2$ is enhanced due to its meta-stable state, with <5% variance in thermoelectric figure of merit (ZT) measurements, and the ZT value is raised from 0.8 to 1.7 at 643 K through the optimized thermal cycling. The findings indicate that thermal cycling is an effective strategy for enhancing the thermal stability and thermoelectric performance of $AgSbTe_2$, presenting a novel approach for achieving uniform secondary phases in materials with phase separation or phase change characteristics.

1. Introduction

Since the direct energy conversion or heat transfer of the thermoelectric device can offer waste heat recovery or eco-friendly solid-state cooling, thermoelectric materials can contribute to increase the energy efficiency or addressing environmental issue of the conventional cooling systems.[1–3] The thermoelectric performance of the device is strongly affected by the material properties such as the thermoelectric figure of merit $ZT = S^2\sigma T/\kappa$, where S, σ, T, and κ are Seebeck coefficient, electric conductivity, absolute temperature, and thermal conductivity, respectively. The parameters S, σ, and κ are strongly related to the carrier concentration (n), and the S and σ are inversely proportional to each other. The κ primarily consists of the electronic contribution(κ_e) and phonon contribution (κ_L). Since these parameters affect each other, achieving a high ZT value is challenging.[1–5]

$AgSbTe_2$ is considered one of the promising thermoelectric materials for high-performance thermoelectric modules in the mid-temperature range (≈400 to 700 K).[6–8] The structure of $AgSbTe_2$ is disordered rock-salt, with Ag and Sb randomly occupying cation sites, and Te occupying anion sites.[9,10] The pristine $AgSbTe_2$ intrinsically shows low thermal conductivity (0.5–0.7 $Wm^{-1}K^{-1}$ near room temperature) due to glass-like phonon scattering associated with the spontaneously formed nanostructure.[7,8,11] Particularly, the thermal

J. H. Kim, J. H. Yun, S. Cha, J.-S. Rhyee
Department of Applied Physics and Institute of Natural Sciences, Integrated Education Institute for Frontier Science and Technology (BK21 Four)
Kyung Hee University
Yongin 17104, Republic of Korea
E-mail: jinheekim@khu.ac.kr; jsrhyee@khu.ac.kr

The ORCID identification number(s) for the author(s) of this article can be found under https://doi.org/10.1002/adfm.202404886

© 2023 The Authors. Advanced Functional Materials published by Wiley-VCH GmbH. This is an open access article under the terms of the Creative Commons Attribution License, which permits use, distribution and reproduction in any medium, provided the original work is properly cited.

DOI: 10.1002/adfm.202404886

S. Byeon, J. Park, H. Jin
Department of Mechanical Engineering
Pohang University of Science and Technology (POSTECH)
Pohang 37673, Republic of Korea

S. Kim, S.-J. Kim
Department of Chemistry and Nano Science
Ewha Womans University
Seoul 03760, Republic of Korea

J. Park, J. Jang, S. Park
Energy Conversion Research Center
Korea Electrotechnology Research Institute (KERI)
Changwon 51543, Republic of Korea

16163028, 2024, 42, Downloaded from https://advanced.onlinelibrary.wiley.com/doi/10.1002/adfm.202404886 by Ewha Womans University Library, Wiley Online Library on [06/04/2025]. See the Terms and Conditions (https://onlinelibrary.wiley.com/terms-and-conditions) on Wiley Online Library for rules of use; OA articles are governed by the applicable Creative Commons License

conductivity of the Cd-doped $AgSbTe_2$ reaches extremely low values of ≈0.28 Wm^{-1} K^{-1} due to the enhanced lattice strain.[7] Additionally, it has the large Seebeck coefficient (≈250 μV K^{-1} near room temperature) by the highly degenerated flat valence bands. These characteristics make $AgSbTe_2$ a good candidate for high-performance thermoelectric material.[10–13] Based on the characteristics, the high ZT values were achieved by the alloying such as the PbTe + $AgSbTe_2$ (LAST, ZT ≈2.2 at 800 K),[14] GeTe + $AgSbTe_2$ (TAGS, ZT ≈1.5 at 720 K)[15] and the doping such as the Cd-doped $AgSbTe_2$ (ZT ≈2.6 at 573 K),[7] the S and Se-doped $AgSbTe_2$ (ZT ≈2.3 at 673 K).[8]

The performance of thermoelectric modules can be affected by the thermoelectric properties of the thermoelectric materials, module structure, contact resistance, diffusion barrier, electrode contact layer, etc.[16–18] Ensuring the phase stability of thermoelectric materials is the first step to achieving the theoretically calculated performance. However, despite the high ZT value, the thermally unstable characteristic of the $AgSbTe_2$ make it difficult to apply in thermoelectric modules operating within the mid-temperature range. Initially, the pristine $AgSbTe_2$ is thermodynamically unstable, decomposing into Sb_2Te_3 and Ag_2Te below 633 K.[19–21] The phase diagram of Sb_2Te_3-Ag_2Te pseudobinary system shows that the $AgSbTe_2$ phase is formed in the temperature range from 633 to 821 K.[19–21] Phase separation into Ag_2Te and Sb_2Te_3, caused by annealing of the $AgSbTe_2$ at 523 K, and the stabilization of the $AgSbTe_2$ phase after annealing at 703 K, support the presence of the metastable $AgSbTe_2$ phase within the Sb_2Te_3-Ag_2Te pseudobinary system.[20] To circumvent this decomposition issue, the suggested application temperature for $AgSbTe_2$ is near room temperature for cooling or above 633 K for waste heat harvesting.[21] The other reason of the unstable $AgSbTe_2$ is the Ag_2Te precipitate that undergoes a phase transition near 418 K. The presence of n-type Ag_2Te makes the p-type $AgSbTe_2$ not only unstable thermally but also decrease the thermoelectric performance.[20,21] Especially, the thermally unstable characteristic of the $AgSbTe_2$ was clearly observed by the repeated measurements of the thermoelectric properties.[20,21] The uncertainties associated with the repeated measurements of the thermoelectric properties were reported to be ≈20% for the ZT values of the Cd-doped $AgSbTe_2$,[7] the S- and Se-doped $AgSbTe_2$.[8] Therefore, the previous experimental results are not sufficient to demonstrate the thermal stability of $AgSbTe_2$.

In this investigation, we discovered that a thermal cycling process can enhance the thermoelectric performance and thermal stability of the $AgSbTe_2$. The high-quality poly crystalline $AgSbTe_2$, exhibiting a clean single phase, includes very small Ag_2Te secondary phase (<5%), as shown in Figure S1a (Supporting Information). Although the Ag_2Te phase is very small, the thermoelectric properties vary among different parts of the $AgSbTe_2$ ingot, as shown in Figure S1b–f (Supporting Information). Additionally, the thermal stability of the S-1 sample (less Ag_2Te, the ZT variance is ≈5%) is much lower than that of the S-2 sample (more Ag_2Te, the ZT variance is ≈30%). The higher ZT variance clearly indicates that the Ag_2Te secondary phase makes the $AgSbTe_2$ more unstable thermally. However, the thermoelectric performance of the S-2 sample was improved with repeated measurements, as shown in Figure S1f (Supporting Information). The results imply that the repeated measurements can be considered as a thermal cycling and can increase the thermoelectric properties of the $AgSbTe_2$. While the thermal cycling has been employed to confirm the thermal stability of thermoelectric modules in the previous studies,[22,23] we utilized it to enhance the thermoelectric performance. Additionally, since the thermal cycling process known as an effective way to enhance the grain refinement of steels,[24–26] it can also lead to homogeneous phase separation of the Ag_2Te or Sb_2Te_3 in the $AgSbTe_2$. Our result show that the thermal cycling makes the secondary phases, such as Sb_2Te_3 and Ag_2Te of the $AgSbTe_2$, more homogeneous. The homogeneous phase separation is considered a meta-stable state with low Gibbs free energy, it can cause the stable phase separation. The enhanced thermal stability of $AgSbTe_2$ due to the optimized thermal cycling condition was confirmed by the repeated thermoelectric property measurements (with the ZT value variance below 5%). Moreover, the optimized thermal cycling condition enabled a high ZT value (1.7 at 643 K) by the enhanced carrier concentrations with the Ag-nano particles and the reduced minority carrier mobility due to the electron carrier localization by the Sb_2Te_3 phase separation.

2. Results and Discussion

2.1. Phase Separation in $AgSbTe_2$

The phase separation with the $AgSbTe_2$ and the secondary phase such as Ag_2Te or Sb_2Te_3 can be described by considering Gibbs free energy change of mixing (ΔG_{mix}) as follow equation.

$$\Delta G_{mix} = \Delta H_{mix} - T\Delta S_{mix} \quad (1)$$

where the ΔH_{mix}, T and ΔS_{mix} are the enthalpy change, absolute temperature, and entropy change of mixing, respectively.[27,28] In the presence of a homogeneous phase separation state within mixed-phase materials, the material characterized by the minimized ΔG_{mix} could exist as a meta-stable state (a local minimum), as depicted in **Figure 1a**. The unstable state represents the randomly mixed state with relatively large grainsize size of Ag_2Te within the $AgSbTe_2$. In the metastable state, the Ag_2Te phase disappears within the $AgSbTe_2$ matrix, and a new phase of Sb_2Te_3 forms uniformly with a small grain size. Because the Gibbs free energy of the homogeneously mixed state with small size of Sb_2Te_3 grains is lower than the energy of the randomly mixed state with large Ag_2Te grains, the $AgSbTe_2$ after the thermal cycling process, including homogeneously mixed small Sb_2Te_3 grains, could be more stable state.

The thermal cycling process is performed to refine the grain of the secondary phase of the $AgSbTe_2$. The stoichiometric ratio of the $AgSbTe_2$ necessarily includes the Ag_2Te phase, and the intrinsic $AgSbTe_2$ phase slowly decomposes to Ag_2Te and Sb_2Te_3 below 633 K,[20,21] as presented in Figure S2 (Supporting Information). The thermoelectric properties are measured for the 1) initial and 2) annealed $AgSbTe_2$. The $AgSbTe_2$ is annealed at 623 K for 100 h to compare the annealing effect with the thermal cycling effect. The thermal cycling effect of the $AgSbTe_2$ was investigated above the decomposition temperature of 633 K. The temperature ranges of the thermal cycling are denoted as "(3) T_{mid} T. C." for the mid-temperature range from room temperature to 643 K and "(4) T_{high} T. C." for the high-temperature range from room temperature to 663 K, as shown in Figure S2 (Supporting

© 2023 The Authors. Advanced Functional Materials published by Wiley-VCH GmbH

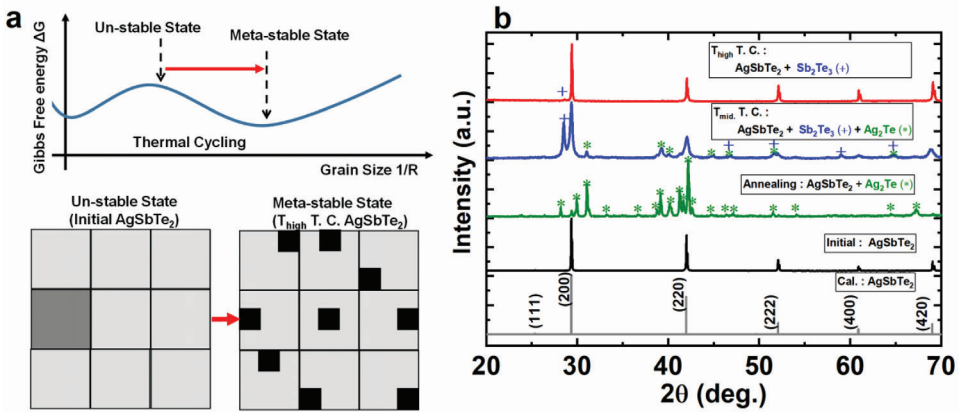


Figure 1. a) Conceptual schematic diagram of Gibbs free energy and phase separation by thermal cycling effect. b) XRD patterns of the calculated (gray), initial (black), annealed (green), T_{mid} T. C. (blue), and T_{high} T. C. (red) $AgSbTe_2$.

information). The maximum thermal cycling temperature for the $AgSbTe_2$ is ≈663 K. The thermoelectric property measurements are not available due to thermal softening of the $AgSbTe_2$ above 663 K.

The powder X-ray diffraction (XRD) patterns of the 1) initial, 2) annealed, 3) T_{mid} T. C., and 4) T_{high} T. C. $AgSbTe_2$ are presented in Figure 1b. The XRD peaks of the 1) initial $AgSbTe_2$ are well matched with the NaCl structure (Space group No. 225, Fm_3m) with the very small Ag_2Te peaks. The lattice parameter of the 1) initial $AgSbTe_2$ (a = 6.07Å) is comparable with the literature values (a = 6.07–6.08 Å).[6,29–32] In contrast, the 2) annealed $AgSbTe_2$ clearly shows small $AgSbTe_2$ peaks with the large Ag_2Te phase, similar to the other literatures.[20,21] However, the XRD peaks of the (3, 4) thermal cycled $AgSbTe_2$ show the Sb_2Te_3 phase. In the case of the 3) T_{mid} T. C. sample, it has the main $AgSbTe_2$ phase with the secondary phases of Sb_2Te_3 and Ag_2Te. The XRD peaks of the 4) T_{high} T. C. sample show the main $AgSbTe_2$ phase with very small Sb_2Te_3 peaks. The high-temperature powder XRD results (from 300 to 673 K) of the $AgSbTe_2$ clearly show that the repeated thermal cycling of the $AgSbTe_2$ generates the Sb_2Te_3 phase separation, as shown in Figure S3 (Supporting Information).

The Ag_2Te secondary phase of the $AgSbTe_2$ is identified through scanning electron microscopy and energy dispersive X-ray spectroscopy (SEM/EDS), as shown in **Figure** 2a. The $AgSbTe_2$ and Ag_2Te phases are distinguished by the different elements ratios in the EDS results. Figure 2b clearly shows that the Ag_2Te secondary phase increases in the 2) annealed $AgSbTe_2$, similar to the XRD results. However, the secondary phases such as Ag_2Te and Sb_2Te_3 of the (3, 4) thermal cycled $AgSbTe_2$ samples are uniformly separated in the $AgSbTe_2$ matrix, as shown in Figure 2c,d. Because the grain sizes of the secondary phases of Ag_2Te and Sb_2Te_3 after the thermal cycling are significantly reduced compared the size of the Ag_2Te in the 1) initial $AgSbTe_2$, the secondary phases after the thermal cycling process, as confirmed the XRD results, were indistinguishable from the $AgSbTe_2$ in the SEM/EXD measurements, as shown in Figure 2c,d. Schematic images describing the annealing and thermal cycling effect are presented for the 1) initial, 2) annealed, 3) T_{mid} T. C., and 4) T_{high} T. C. $AgSbTe_2$ in Figure 2e–h. The

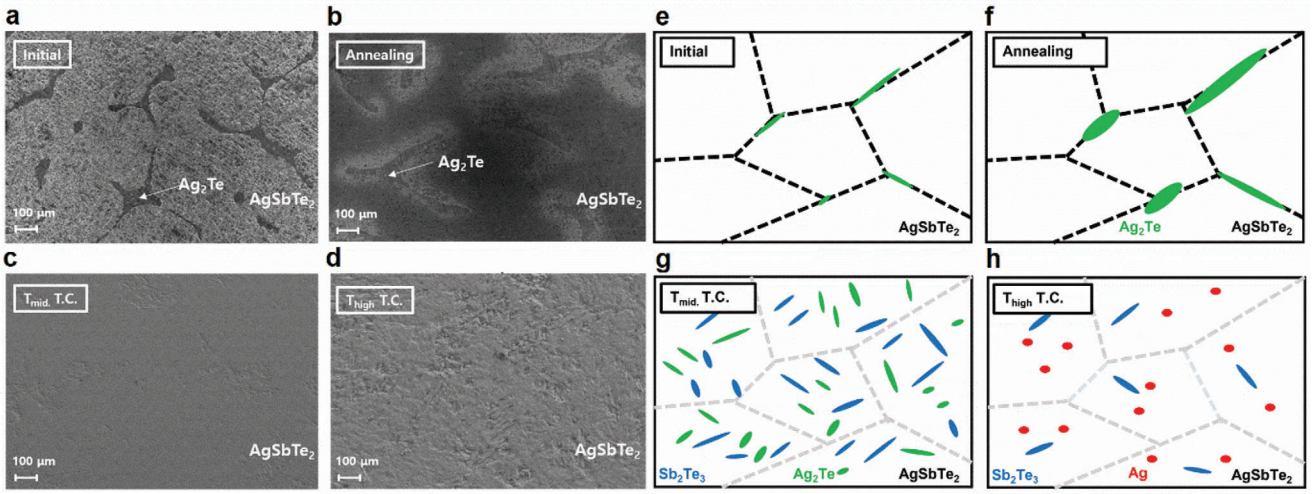


Figure 2. SEM images and schematic diagrams of the a,e) initial, b,f) annealed, c,g) T_{mid} T. C., and d,h) T_{high} T. C. $AgSbTe_2$.

© 2023 The Authors. Advanced Functional Materials published by Wiley-VCH GmbH

16163028, 2024, 42, Downloaded from https://advanced.onlinelibrary.wiley.com/doi/10.1002/adfm.202404886 by Ewha Womans University Library, Wiley Online Library on [06/04/2025]. See the Terms and Conditions (https://onlinelibrary.wiley.com/terms-and-conditions) on Wiley Online Library for rules of use; OA articles are governed by the applicable Creative Commons License

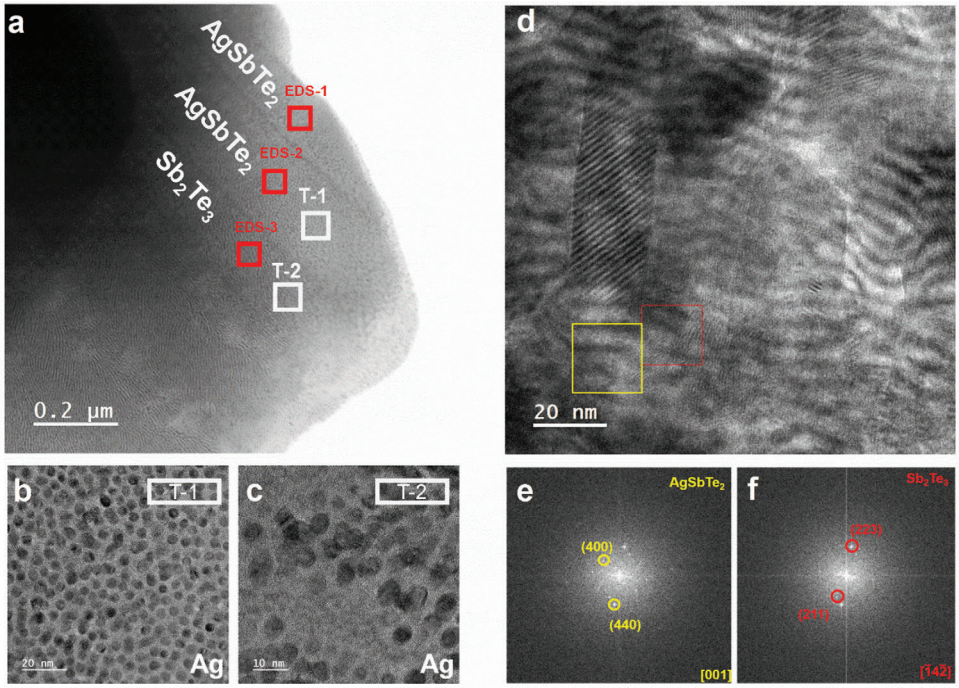


Figure 3. a) TEM image of the plate-like Sb_2Te_3 phase separation, b,c) Ag-nano particles, d) TEM image, and e,f) FFT patterns of the T_{high} T. C. $AgSbTe_2$.

SEM/EDS measurement results clearly shows that the thermal cycling is effective in refining the graine size of the secondary phase of the $AgSbTe_2$.

The reduced grains of the secondary phase after the thermal cycling are recognized through transmission electron microscope (TEM) measurements. In the (4) T_{high} T. C. $AgSbTe_2$ sample, the Sb_2Te_2 and $AgSbTe_2$ are distinguished by the atomic ratios from the EDS measurements and it shows a plate-like shape as shown in **Figure 3**a. The Sb and Te atomic ratios in Table S1 (Supporting Information) roughly match the Sb_2Te_3 (Sb:Te = 2:2.8) and $AgSbTe_2$ (Sb:Te = 1:1.84). The plate-like Sb_2Te_3 secondary phase of a few micrometers in scales was found in literature regarding annealing studies of $AgSbTe_2$.[31,33] The formation of the plate-like Sb_2Te_3 in the (4) T_{high} T. C. $AgSbTe_2$ is caused by the heat treatment during the heat cycling. The fast-Fourier-transform (FFT) patterns of the (4) T_{high} T. C. $AgSbTe_2$ sample clearly shows the $AgSbTe_2$ and Sb_2Te_3 phase as shown in Figure 3e,f. However, the Ag elements are homogeneously precipitated as nanoparticles, which is confirmed by the TEM measurement as shown in Figure 3b,c. The presence of Ag nanoparticles is confirmed by the higher Ag element ratio of the EDS results. Additionally, the FFT patterns of the TEM image and the high-angle annular dark-field scanning transmission electron microscopy (HAADF-STEM) image in Figure S4 (Supporting Information) indicate that the Ag nano particles exist in the (4) T_{high} T. C. $AgSbTe_2$ sample.

2.2. Thermoelectric Properties

Figure 4a shows temperature-dependent electrical resistivities ρ(T) for the initial measurement and the thermal cycling of the $AgSbTe_2$. All measured data of the electrical resistivities are presented in Figure S5a (Supporting Information). The electrical resistivity (9.9 mΩ cm near room temperature) of the 1) initial measurement is comparable to the literature values (7–10 mΩ cm near room temperature) of the pristine $AgSbTe_2$.[6–8] The electrical resistivities are continuously decrease with repeated measurements in the temperature range from room temperature to 643 K, denoted as the 3) T_{mid} T. C. The decreasing trend of ρ(T) due to the thermal cycling are saturated after several times of thermal cycling as shown in Figure 4b. With the enhanced maximum thermal cycling temperature from 643 to 663 K, the 4) T_{high} T. C. $AgSbTe_2$ exhibits stable electrical resistivities, showing within 3% variance. The thermal stability of the electrical resistivities of the 4) T_{high} T. C. $AgSbTe_2$ is significantly improved compared to previous studies.[6–8] The enhanced thermal stability of the electrical resistivity with the increased thermal cycling temperature is attributed to the $AgSbTe_2$ recombination, as revealed in the XRD results.

Additionally, the thermoelectric properties of the annealed $AgSbTe_2$ at 643 and 663 K for 100 h were examined to distinguish between the annealing and thermal cycling effect. The annealing temperatures are similar to the maximum temperature of the thermal cycling process, denoted as the 3) T_{mid} T. C. and 4) T_{high} T. C. The electrical resistivities of the annealed $AgSbTe_2$ samples are not similar to the resistivity of the thermal cycled samples as shown in Figure S6 (Supporting Information). The broad humps of the resistivity are enhanced and clearly appeared near 500 K in the annealed $AgSbTe_2$ at 643 and 663 K. The broad humps near 500 K are mainly affected by the Ag_2Te precipitation in the $AgSbTe_2$.[31] The broad hump in the electrical resistivity, as shown Figure S6a,b (Supporting Information), indicates the Ag_2Te phase separation in the $AgSbTe_2$. However,

© 2023 The Authors. Advanced Functional Materials published by Wiley-VCH GmbH

16163028, 2024, 42, Downloaded from https://advanced.onlinelibrary.wiley.com/doi/10.1002/adfm.202404886 by Ewha Womans University Library, Wiley Online Library on [06/04/2025]. See the Terms and Conditions (https://onlinelibrary.wiley.com/terms-and-conditions) on Wiley Online Library for rules of use; OA articles are governed by the applicable Creative Commons License

16163028, 2024, 42, Downloaded from https://advanced.onlinelibrary.wiley.com/doi/10.1002/adfm.202404886 by Ewha Womans University Library, Wiley Online Library on [06/04/2025]. See the Terms and Conditions (https://onlinelibrary.wiley.com/terms-and-conditions) on Wiley Online Library for rules of use; OA articles are governed by the applicable Creative Commons License

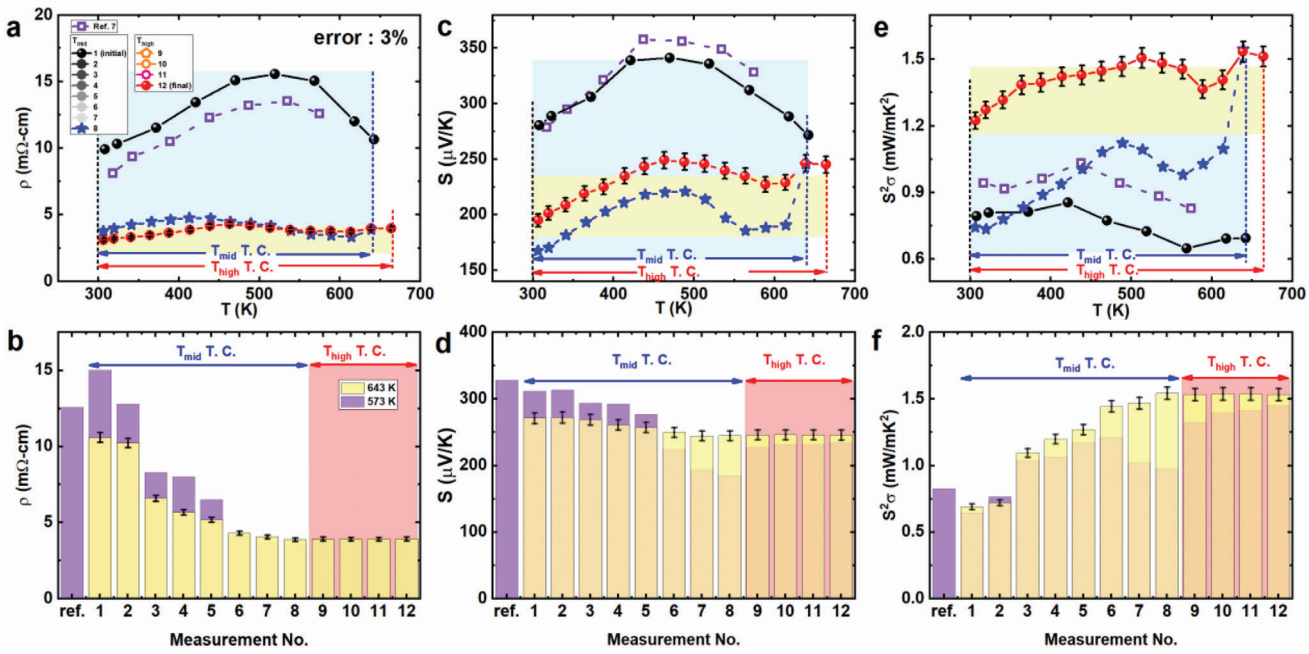


Figure 4. a) Temperature-dependent electrical resistivities, c) Seebeck coefficients and e) power factors of the T_{mid} T. C. and T_{high} T. C. $AgSbTe_2$ and b) Electrical resistivities, d) Seebeck coefficients and f) power factors at 537 and 643 K.

the first measurement of the electrical resistivity after annealing at 643 K shows a small broad hump that means fewer Ag_2Te phase separations. The broad humps after annealing at 643 K are enhanced with increasing measurement times, but the broad humps after annealing at 663 K do not change significantly. These behaviors suggest that an unknown and unstable phase of the $AgSbTe_2$ may exist near 643 K. Based on the unstable state of the $AgSbTe_2$ near 643 K, the meta-stable state can be generated through the thermal cycling process. And the electrical resistivities of the annealed $AgSbTe_2$ clearly shows that the annealing effect of the $AgSbTe_2$ is not same with the thermal cycling effect, and the Ag_2Te cannot be removed by the simple annealing process.

Since the electrical resistivity of the $AgSbTe_2$ is highly sensitive to the secondary phases, the thermal stability of the $AgSbTe_2$ after the thermal cycling process is confirmed by ten consecutive measurements of the electrical resistivity at each measurement temperature with increasing temperature, as shown Figure S7 (Supporting Information). The normalized $\rho_N(\rho/\rho_{300K})$ indicates the thermal stability of the $AgSbTe_2$ at each measurement temperature. Unlike the higher variations in the resistivity of the 1) initial $AgSbTe_2$, the low variations in the 4) $AgSbTe_2$ after the thermal cycling process clearly show the enhanced thermal stability due to the thermal cycling process.

Temperature-dependent Seebeck coefficients S(T) for the initial measurement and the thermal cycling of the $AgSbTe_2$ are presented in Figure 4c. All measured data of the Seebeck coefficients are included in Figure S5b (Supporting Information). The Seebeck coefficient (280 μV K^{-1} near room temperature) of the 1) initial measurement is similar to the literature values (265–278 μV K^{-1} near room temperature) of the pristine $AgSbTe_2$.[6–8] The Seebeck coefficients are continuously decrease with the repeated measurements for the 3) T_{mid} T. C. and then are enhanced by the 4) T_{high} T. C. The Seebeck coefficients for the 4) T_{high} T. C. $AgSbTe_2$ are stable for the repeated measurements within 3% variance. The decreasing Seebeck coefficients of the 3) T_{mid} T. C. $AgSbTe_2$ are related to the phase decomposition from $AgSbTe_2$ to Sb_2Te_3 and Ag_2Te. The enhanced Seebeck coefficients by the 4) T_{high} T. C. are affected by the $AgSbTe_2$ recombination without Ag_2Te, which exhibits the negative Seebeck coefficients.[31]

The Seebeck coefficients of the 1) initial $AgSbTe_2$ decrease with increasing temperature above 500 K. The decreased Seebeck coefficients is due to the bipolar effect which is caused by the narrow bandgap of the $AgSbTe_2$.[6,32] However, the enhancements of the Seebeck coefficients above 600 K are observed in the $AgSbTe_2$ after the thermal cycling. Additionally, the enhanced Seebeck coefficients above 550 K is founded in the composite with the $AgSbTe_2$ and Sb_2Te_3.[31] The enhanced Seebeck coefficients of the $AgSbTe_2$ after the thermal cycling in the high-temperature range may be affected by the band convergence due to the Sb_2Te_3 secondary phase.

The effect of the Ag_2Te in the $AgSbTe_2$ on the Seebeck coefficient is confirmed through comparison of the bulk Seebeck coefficients and local Seebeck coefficients. Using the mapping measurement for the local Seebeck coefficient, we found that the local Seebeck coefficients of the 1) initial $AgSbTe_2$ (with Ag_2Te, local $S_{avr.}$ ≈128 μV K^{-1}) are much lower than the values of the 4) T_{high} T. C. $AgSbTe_2$ (No Ag_2Te, local $S_{avr.}$ ≈180 μV K^{-1}), as shown in Figure S8 (Supporting Information). The lower local Seebeck coefficients of the 1) initial $AgSbTe_2$ contrast with the higher bulk Seebeck coefficients of the 1) initial $AgSbTe_2$ (bulk S = 280 μV K^{-1} at room temperature) compare with the bulk Seebeck coefficients of the (4) T_{high} T. C. $AgSbTe_2$ (bulk S = 195 μV K^{-1} at room temperature). The Seebeck coefficient mapping results indicate that

© 2023 The Authors. Advanced Functional Materials published by Wiley-VCH GmbH

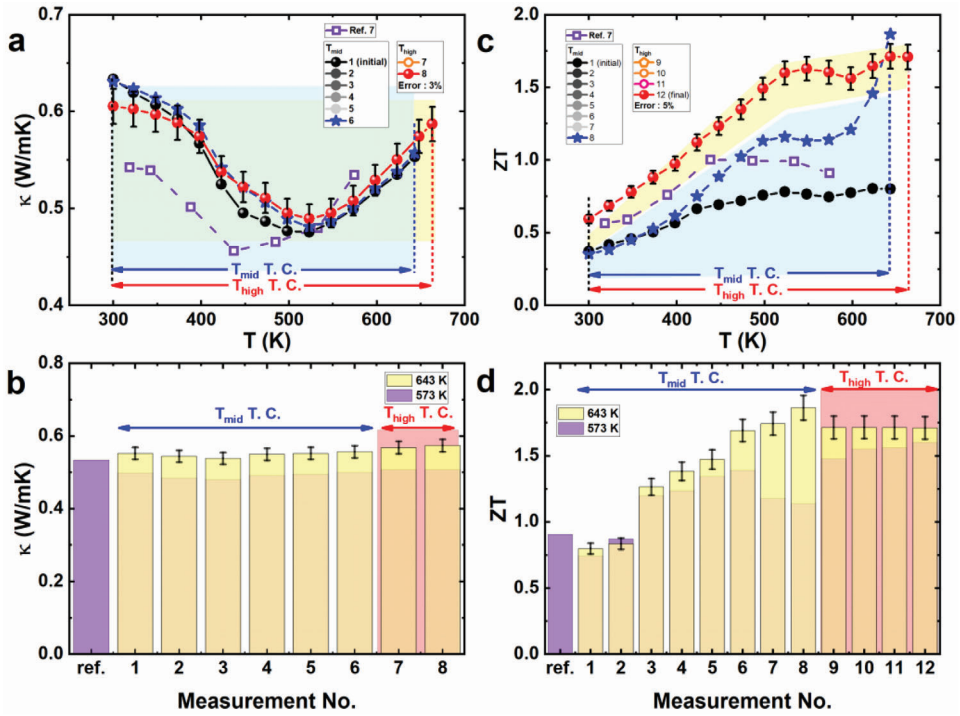


Figure 5. a) Temperature dependent thermal conductivities and c) ZT values of the T_{mid} T. C. and T_{high} T. C. $AgSbTe_2$ and b) thermal conductivities, and d) ZT values at 537 and 643 K.

the n-type Ag_2Te locally distributed and decreases the local Seebeck coefficients in the initial $AgSbTe_2$.

The decreased Seebeck coefficients of the 4) T_{high} T.C. $AgSbTe_2$, comparing to the values of the initial sample, is primarily due to the enhanced carrier concentration from the Ag nano-particles, not Ag_2Te. The absence of the Ag_2Te in the 4) T_{high} T.C. $AgSbTe_2$ is supported by the electrical resistivity results. The broad hump in the electrical resistivity near 500 K and Anderson localization near 180 K indicate that the electrical resistivity can be affected by the Ag_2Te in the $AgSbTe_2$. Those effects will be discussed in more detail later.

Temperature-dependent power factors $S^2\sigma(T)$ for the initial measurement and the thermal cycling of the $AgSbTe_2$ are clearly enhanced by the thermal cycling, as shown Figure 4e. All obtained power factors are presented in Figure S5c (Supporting Information). The power factor (0.8 mWm^{-1} K^{-2} near room temperature) of the 1) initial measurement is comparable to the power factors of the pristine $AgSbTe_2$ (0.65–0.95 mWm^{-1} K^{-2} near room temperature) in the literatures.[6–8] The power factors of the 3) T_{mid} T. C. are enhanced above the $AgSbTe_2$ composition temperature (633 K), but the power factors of the 4) T_{high} T. C. are enhanced in the whole measured temperature range compared to the 1) initial measurement. The enhanced power factors clearly show that the thermal cycling can increase the power factor, mainly caused by the decreasing electrical resistivity. Also, the stable power factors by the 4) T_{high} T. C. are presented in Figure 4f within 3% variance.

Temperature-dependent thermal conductivities for the initial measurement and the thermal cycling of the $AgSbTe_2$ are shown in **Figure** 5a. All measured thermal conductivities are presented in Figure S5d (Supporting Information). The thermal conductivity of the initial measurement of the $AgSbTe_2$ is 0.63 Wm^{-1} K^{-1}, which falls within the range of 0.5–0.7 Wm^{-1} $K^{-1}$of the pristine $AgSbTe_2$ near room temperature in the literatures.[6–8,12] The thermal conductivities by the thermal cycling dose not changed significantly and are stable at high temperature range as shown in Figure 5b. The thermal conductivities for the 4) T_{high} T. C. are within 3% variance.

The thermal conductivity(κ) is primarily affected by the phonon (κ_L), electronic (κ_e) and bipolar diffusion contribution(κ_b). The electronic thermal conductivity(κ_e) can be obtained using the Wiedemann–Franz law ($\kappa_e = L\sigma T$, where L is the Lorenz number, σ is the electrical conductivity and T is the absolute temperature). The Lorenz numbers for a degenerated semiconductor are calculated using the temperature-dependent Seebeck coefficients.[7,34,35] The calculated Lorenz numbers of the $AgSbTe_2$ are presented in Figure S9a (Supporting Information). The Lorenz numbers for the initial measurement and thermal cycling of the $AgSbTe_2$ are comparable with the literature values.[7,8] The lattice (κ_L) and bipolar thermal conductivity (κ_b) are obtained by subtracting the electronic thermal conductivity(κ_e) from the measured thermal conductivity(κ). The temperature-dependent lattice and bipolar thermal conductivities ($\kappa_L + \kappa_b$) are presented in Figure S9b (Supporting Information). The temperature-dependent lattice thermal conductivities (κ_L) decrease with increasing temperature due to the enhanced phonon scattering, whereas the bipolar thermal conductivities (κ_b) increase with increasing temperature due to enhanced bipolar diffusion at high temperature.[7,8,34,35] Because the increased thermal conductivity due to the bipolar effect

© 2023 The Authors. Advanced Functional Materials published by Wiley-VCH GmbH

16163028, 2024, 42, Downloaded from https://advanced.onlinelibrary.wiley.com/doi/10.1002/adfm.202404886 by Ewha Womans University Library, Wiley Online Library on [06/04/2025]. See the Terms and Conditions (https://onlinelibrary.wiley.com/terms-and-conditions) on Wiley Online Library for rules of use; OA articles are governed by the applicable Creative Commons License

16163028, 2024, 42, Downloaded from https://advanced.onlinelibrary.wiley.com/doi/10.1002/adfm.202404886 by Ewha Womans University Library, Wiley Online Library on [06/04/2025]. See the Terms and Conditions (https://onlinelibrary.wiley.com/terms-and-conditions) on Wiley Online Library for rules of use; OA articles are governed by the applicable Creative Commons License

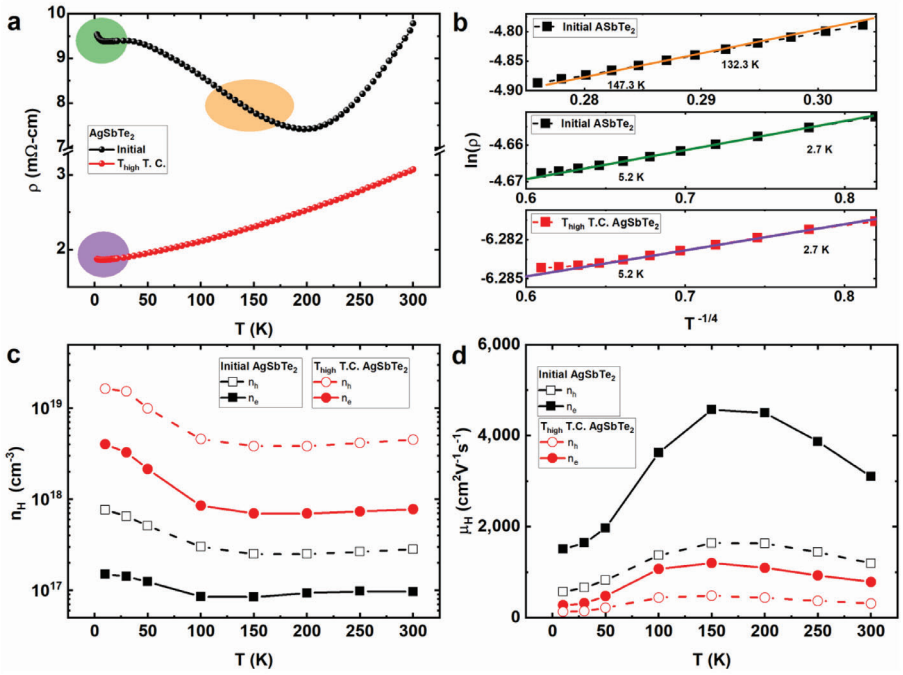


Figure 6. a) Temperature dependent electrical resistivities, b) linear fit by Mott 3D VRH, c) Hall carrier concentrations of electron and hole, and d) Hall mobilities of the initial and T_{high} T. C. $AgSbTe_2$ below room temperature.

appears above 500 K, the lattice thermal conductivity (κ_L) of the $AgSbTe_2$ is dominant near room temperature. The lattice thermal conductivities (κ_L) of the $AgSbTe_2$ after the thermal cycling process are significantly reduced compared to the values of the 1) initial $AgSbTe_2$. The reduced lattice thermal conductivities indicate that the secondary phases due to the thermal cycling process effectively reduce the lattice thermal conductivity of the $AgSbTe_2$.

Figure 5c presents the temperature-dependent figure of merit ZT for the initial measurement and the thermal cycling of the $AgSbTe_2$. All data of the ZT values are presented in Figure S5e (Supporting Information). The ZT value (0.35) of the initial $AgSbTe_2$ is comparable to the ZT values of the pristine $AgSbTe_2$ (0.3–0.5 near room temperature) in the literatures.[6–8] The ZT values are significantly enhanced from 0.8 to 1.7 at 643 K by the thermal cycling and show the stable behavior in the repeated measurements, presenting similar values within 5% variance, as shown Figure 5d. The enhanced ZT values of the 4) T_{high} T. C. mainly caused by the remarkably decreased electrical resistivity due to the thermal cycling.

2.3. Electrical Transport Properties

The low-temperature electrical resistivities for the 1) initial and the 4) T_{high} T. C. $AgSbTe_2$ are presented in **Figure 6a**. The increasing electrical resistivities with decreasing temperature appear near 5 and 180 K in the 1) initial $AgSbTe_2$ sample and near 5 K in the 4) T_{high} T. C. $AgSbTe_2$. The electrical resistivity minimum of the 1) initial $AgSbTe_2$ near 180 K is similar to the resistivity minimum of the pristine $AgSbTe_2$ near 170 K in the literature.[10] The resistivity minimums of the 1) initial and 4) T_{high} T. C. $AgSbTe_2$ near 5 K are comparable to the resistivity minimum of the Cd-doped AgSbTe2 near 10 K.[7] The activation energy can be obtained from the increasing electrical resistivity with decreasing temperature using the Arrhenius equation:

$$\rho \propto exp\left(\frac{-E_a}{k_B T}\right) \tag{2}$$

where ρ is the electrical resistivity, E_a is the activation energy, k_B is the Boltzmann constant and T is the absolute temperature.[36,37] In the case of the resistivity of the 1) initial $AgSbTe_2$ near 180 K, the activation energy is estimated to be ≈3.2 meV (the fitting temperature range: 127–182 K), which is comparable to the activation energy of 1–2 meV of the $AgSbTe_2$.[10] For the resistivity of the 1) initial and the 4) T_{high} T. C. $AgSbTe_2$ near 5 K, the estimated activation energies are ≈5.3 μeV (fitting temperature range: 3.2–6.7 K for the of the 1) initial $AgSbTe_2$) and 1.2 μeV (fitting temperature range: 3.2–6.7 K for the 4) T_{high} T. C. $AgSbTe_2$), respectively. The reduced activation energy of the 4) T_{high} T. C. $AgSbTe_2$ comparing to the values of the 1) initial $AgSbTe_2$ means that the Ag-Sb cation disorder is reduced by the thermal cycling process.

The origin of the electrical resistivity minimum of the $AgSbTe_2$ can be explained by disorder-induced electronic localization known as Anderson localization.[7] The $AgSbTe_2$ exhibits two different types of disorder: disordered impurity phases (Ag_2Te or Sb_2Te_3) and cationic disorder (Ag or Sb).[7,9,10,38] The resistivity minimum near 180 K of the 1) initial $AgSbTe_2$ can be attributed to the Ag_2Te secondary phase in the $AgSbTe_2$. In contrast, the resistivity minimum near 180 K is not appear in the 4) T_{high} T. C. $AgSbTe_2$ which is not include the Ag_2Te. Also, the resistivity minimum of the 1) initial and 4) T_{high} T. C. $AgSbTe_2$ near 5 K can be

© 2023 The Authors. Advanced Functional Materials published by Wiley-VCH GmbH

considered an Ag-Sb cation disorder effect. The resistivity minimum due to Ag-Sb cation disorder is supported by the results of the Cd-doped $AgSbTe_2$, showing the resistivity minimum caused by the cation ordering near 10 K.[7]

The thermally activated electrons in the disordered system exhibit variable range hopping (VRH) behavior, defined by the following equation:[39–41]

$$\rho\ (T) = \rho_0\ exp\left(\frac{T_0}{T}\right)^{\frac{1}{D+1}} \quad (3)$$

where ρ_0, T_0, T, and D are a pre-exponential factor, a characteristic temperature, absolute temperature and dimensionality of the system, respectively. Since the $AgSbTe_2$ has an isotropic cubic structure, the D = 3 for the 3D-VHR is used. The increasing electrical resistivities with decreasing temperature of the 1) initial and the 4) T_{high} T. C. $AgSbTe_2$ exhibit the 3D-VRH behavior, as shown Figure 6b. Therefore, electrical resistivity minimum of the 1) initial and the 4) T_{high} T. C. $AgSbTe_2$ can be attributed to the Anderson localization effect of the randomly distributed Ag_2Te phase near 180 K and the Ag-Sb cation disorder near 5 K.

The electrical transport of the intrinsic $AgSbTe_2$ is affected by two-types of carriers: heavy holes (lower hole mobility) with higher hole carrier concentrations and the light electrons (higher electron mobility) with lower electron carrier concentrations.[7,13] To investigate the electrical resistivity change of the $AgSbTe_2$ due to the thermal cycling, the carrier concentrations (n_e, n_h) and mobilities (μ_e, μ_h) of the electron and hole are calculated using two-carrier model[7,13] with the measured longitudinal electrical resistivity ρ_{xx}(H) and Hall resistivity ρ_{xy}(H) under the various magnetic fiends from −5 T to 5 T, as shown in Figure S10 (Supporting Information). The calculated carrier concentrations and mobilities of electron and hole for the 1) initial and 4) T_{high} thermal cycled $AgSbTe_2$ are presented in Figure 6c,d. Similar to the previous investigations,[7,13] the 1) initial $AgSbTe_2$ exhibits lower hole mobility ($\mu_h = 1198\ cm^2\ V^{-1}\ s^{-1}$ at 300 K) with higher hole carrier concentration ($n_h = 2.8 \times 10^{17}\ cm^{-3}$ at 300 K) and higher electron mobility ($\mu_e = 3101\ cm^2\ V^{-1}\ s^{-1}$ at 300 K) with lower electron carrier concentration ($n_e = 9.6 \times 10^{16}\ cm^{-3}$ at 300 K). The 4) T_{high} T. C. $AgSbTe_2$ also shows a similar behavior with lower hole mobility ($\mu_h = 314\ cm^2\ V^{-1}\ s^{-1}$ at 300 K) with higher hole carrier concentration ($n_h = 4.5 \times 10^{18}\ cm^{-3}$ at 300 K) and higher electron mobility ($\mu_e = 788\ cm^2\ V^{-1}\ s^{-1}$ at 300 K) with lower electron concentration ($n_e = 7.8 \times 10^{17}\ cm^{-3}$ at 300 K).

The temperature-dependent carrier concentrations and mobilities of the 1) initial and 4) T_{high} T. C. $AgSbTe_2$ are not show intrinsic behavior in contrast to the intrinsic behaviors in the transport properties of the pure $AgSbTe_2$.[13] The extrinsic behavior in the carrier concentrations and mobilities are also founded in the highly doped $AgSbTe(Se, S)_2$ samples and the $AgSbTe_2$ including the secondary phase.[7,8] Therefore, the abnormal behavior of the transport properties of the 1) initial and 4) T_{high} T. C. $AgSbTe_2$ is mainly due to the secondary phases. The enhanced electron and hole carrier concentrations of the 4) T_{high} T. C. $AgSbTe_2$ are mainly affected by the Ag-nano particles and the p-type Sb_2Te_3 secondary phase ($n_h = \approx 1 \times 10^{19–20}\ cm^{-3}$).[42,43] The electron and hole mobilities of the 4) T_{high} T. C. $AgSbTe_2$ are decreased due to the enhanced carrier concentrations.

3. Conclusion

In summary, the $AgSbTe_2$ was synthesized by the conventional melting method. We found that the unstable thermoelectric properties of the $AgSbTe_2$ are caused by the Ag_2Te secondary phase, which is a phase-change material. The small amount Ag_2Te of the initial $AgSbTe_2$ affected the low-temperature electrical resistivity, resulting in the appearance of the electrical resistivity minimum near 180 K in the initial $AgSbTe_2$. The Ag_2Te in the $AgSbTe_2$ makes not only the sample unstable in the repeated high-temperature measurements but also increase the electrical resistivity due to Anderson localization.

The enhanced thermal stability of the $AgSbTe_2$ was caused by the repeated measurements, which can be considered as the thermal cycling effect. The optimized thermal cycling condition of the $AgSbTe_2$ increased the variance of the ZT values <5%. The improved thermal stability of the $AgSbTe_2$ can be attributed to the meta-stable state caused by the graine refinement of the secondary phase through the thermal cycling process.

The enhanced thermoelectric performance under the optimized thermal cycling condition was mainly caused by the enhanced power factor with the decreased electrical resistivity. The electrical resistivity of the initial $AgSbTe_2$ decreased due to the increased electron and hole carrier concentrations influenced by the Ag-nano particles after the optimized thermal cycling. As a result, the maximum ZT value of the $AgSbTe_2$ was enhanced from 0.8 to 1.7 at 643 K after the optimized thermal cycling.

4. Experimental Section

Synthesis of $AgSbTe_2$: The high-quality polycrystalline $AgSbTe_2$ ingot was synthesized by the conventional melting method using a rocking furnace. Stoichiometric amounts of Ag (99.999%), Sb (99.999%), and Te (99.999%) were sealed in evacuated quartz tubes under high vacuum. The quartz ampoules were heated to 1123 K and maintained at this temperature for 12 h using a rocking furnace. The melted $AgSbTe_2$ was slowly cooled to room temperature for 2 days.

Phase and Structure Characterization: The X-ray diffraction (XRD) patterns were obtained at room-temperature and high-temperature (from 300 to 673 K) using a D8 advance diffractometer (Bruker, Germany) and an X'Pert PRO diffractometer (PANanalytical, Netherland) with Cu-$\kappa\alpha$ radiation, respectively. The microstructure images and elemental mapping were investigated using a high-resolution field-emission scanning electron microscope with an energy-dispersive X-ray (EDX) spectroscopy (MERLIN, Carl Zeiss, Germany). The nanostructure analysis was performed using a transmission electron microscope (TEM, JEM- ARM-200F, JEOL, Japan).

Electrical and Thermal Transport Property Measurements: The temperature-dependent electrical resistivities (ρ) and Seebeck coefficients (S) were simultaneously measured under helium atmosphere by a four-point probe method using a thermoelectric properties measurement system (ZEM-3, ULVAC-RIKO, Japan) from 300 to 673 K. Seebeck coefficient mapping measurements were performed with 100 µm intervals using a scanning thermal probe micro-imaging apparatus (STPM-1000, Advance Riko, Inc., Japan) at room temperature. The temperature-dependent electrical resistivities (ρ), the longitudinal electrical resistivities (ρ_{xx}(H)), and Hall resistivities (ρ_{xy}(H)) with z-direction magnetic fields (from −5 T to 5 T) were measured by a four-point probe method using the physical properties measurement system (PPMS-14T Dynacool, Quantum Design, USA) from 2 to 300 K. The electron (n_e) and hole (n_h) carrier concentration and electron (μ_e) and hole (μ_h) mobility were estimated by a two-carrier model[5,11] with the measured longitudinal

© 2023 The Authors. Advanced Functional Materials published by Wiley-VCH GmbH

16163028, 2024, 42, Downloaded from https://advanced.onlinelibrary.wiley.com/doi/10.1002/adfm.202404886 by Ewha Womans University Library, Wiley Online Library on [06/04/2025]. See the Terms and Conditions (https://onlinelibrary.wiley.com/terms-and-conditions) on Wiley Online Library for rules of use; OA articles are governed by the applicable Creative Commons License

electrical resistivities (ρ_{xx}(H)) and Hall resistivities (ρ_{xy}(H)). The temperature-dependent total thermal conductivities (κ) were calculated by the relation of $\kappa = \rho_s \lambda Cp$, where ρ_s is the sample density, λ is the thermal diffusivity and Cp is the specific heat. The thermal diffusivity is measured by a laser flash method (LFA-456, NETZSCH, Germany). As the specific heat of the $AgSbTe_2$ shows a good agreement with the Dulong-Petit value,[6,7] the Dulong-Petit value was used for the specific heat.

Supporting Information

Supporting Information is available from the Wiley Online Library or from the author.

Acknowledgements

J.H.K. and J.H.Y. contributed equally to this work. This research was supported by the National Research Foundation of Korea (NRF) funded by the Ministry of Education, Science and Technology (RS-2023-00247622 and NRF-2022M3C1A3091988). [Correction added on May 13, 2024, after first online publication: The funding information was corrected.]

Conflict of Interest

The authors declare no conflict of interest.

Data Availability Statement

The data that support the findings of this study are available from the corresponding author upon reasonable request.

Keywords

$AgSbTe_2$, Gibbs free energy, phase stability, thermal cycling, thermal stability, thermoelectric materials

Received: March 21, 2024
Revised: April 23, 2024
Published online: May 8, 2024

[1] X. L. Shi, J. Zou, Z. G. Chen, *Chem. Rev.* **2020**, *120*, 7399.
[2] Z. Wu, S. Zhang, Z. Liu, E. Mu, Z. Hu, *Nano Energy* **2022**, *91*, 106692.
[3] J. Mao, G. Chen, Z. Ren, *Nat. Mater.* **2021**, *20*, 454.
[4] S. Singh, K. Hirata, S. K. Pandey, T. Takeuchi, in *Emerging Materials*, (Eds: L. R. Thoutam, S. Tayal, J. Ajayan), Springer, Singapore **2022**, pp 184.
[5] L. Yang, Z. Chen, M. S. Dargusch, J. Zou, *Adv. Energy Mater.* **2018**, *8*, 1701797.
[6] S. Roychowdhury, R. Panigrahi, S. Perumal, K. Biswas, *ACS Energy Lett.* **2017**, *2*, 349.
[7] S. Roychowdhury, T. Ghosh, R. Arora, M. Samanta, L. Xie, N. K. Singh, A. Soni, J. He, U. V. Waghmare, K. Biswas, *Science* **2021**, *371*, 722.
[8] Y. Zhang, Z. Li, S. Singh, A. Nozariasbmarz, W. Li, A. Genc, Y. Xia, L. Zheng, S. H. Lee, S. K. Karan, G. K. Goyal, N. Liu, S. M. Mohan, Z. Mao, A. Cabot, C. Wolverton, B. Poudel, S. Priya, *Adv. Mater.* **2023**, *35*, 2208994.
[9] E. Quarez, K. F. Hsu, R. Pcionek, N. Frangis, E. K. Polychroniadis, M. G. Kanatzidis, *J. Am. Chem. Soc.* **2005**, *127*, 9177.
[10] K. Hoang, S. D. Mahanti, J. R. Salvador, M. G. Kanatzidis, *Phys. Rev. Lett.* **2007**, *99*, 156403.
[11] J. Ma, O. Delaire, A. F. May, C. E. Carlton, M. A. McGuire, L. H. VanBebber, D. L. Abernathy, G. Ehlers, T. Hong, A. Huq, W. Tian, V. M. Keppens, Y. Shao-Horn, B. S. Sales, *Nat. Nanotechnol.* **2013**, *8*, 445.
[12] D. T. Morelli, V. Jovovic, J. P. Heremans, *Phys. Rev. Lett.* **2008**, *101*, 035901.
[13] V. Jovovic, J. P. Heremans, *Phys. Rev. B* **2008**, *77*, 245204.
[14] K. F. Hsu, S. Loo, F. Guo, W. Chen, J. S. Dyck, C. Uher, T. Hogan, E. K. Polychroniadis, M. G. Kanatzidis, *Science* **2004**, *303*, 818.
[15] S. H. Yang, T. J. Zhu, T. Sun, J. He, S. N. Zhang, X. B. Zhao, *Nanotechnology* **2008**, *19*, 245707.
[16] A. K. R. Ang, I. Yamazaki, K. Hirata, S. Singh, M. Matsunami, T. Takeuchi, *ACS Appl. Mater. Interfaces* **2023**, *15*, 46962.
[17] H. Lai, S. Singh, Y. Peng, K. Hirata, M. Ryu, A. K. R. Ang, L. Miao, T. Takeuchi, *ACS Appl. Mater. Interfaces* **2022**, *14*, 38642.
[18] W. Li, G. K. Goyal, D. Stokes, L. Raman, S. Ghosh, S. Sharma, A. Nozariasbmarz, N. Liu, S. Singh, Y. Zhang, B. Poudel, S. Priya, *ACS Appl. Mater. Interfaces* **2023**, *15*, 2961.
[19] J. D. Sugar, D. L. Medlin, *J. Alloys Compd.* **2009**, *478*, 75.
[20] P. M. Wyzga, K. T. Wojciechowski, *J. Electron. Mater.* **2016**, *45*, 1548.
[21] J. Cao, J. Dong, K. Saglik, D. Zhang, S. F. D. Solco, I. J. W. J. You, H. Liu, Q. Zhu, J. Xu, J. Wu, F. Wei, Q. Yan, A. Suwardi, *Nano Energy* **2023**, *107*, 108118.
[22] M. T. Barako, W. Park, A. M. Marconnet, M. Asheghi, K. E. Goodson, *J. Electron. Mater.* **2013**, *42*, 372.
[23] S. Harish, D. Sivaprahasam, B. Jayachandran, R. Gopalan, G. Sundararajan, *Energy Convers Manag* **2021**, *232*, 113900.
[24] M. Park, A. Shibata, N. Tsuji, *Front. Mater.* **2020**, *7*, 604792.
[25] J. Hidalgo, M. J. Santofimia, *Metall. Mater. Trans. A* **2016**, *47*, 5288.
[26] A. Shibata, S. Daido, D. Terada, N. Tsuji, *Mater. Trans.* **2013**, *54*, 1570.
[27] M. Yanagisawa, *Biophys. Rev.* **2022**, *14*, 1093.
[28] H. W. Luan, Y. Shao, J. F. Li, W. L. Mao, Z. D. Han, C. Shao, K. F. Yao, *Scr. Mater.* **2020**, *179*, 40.
[29] R. Mohanraman, R. Sankar, F. C. Chou, C. H. Lee, Y. Y. Chen, *J. Appl. Phys.* **2013**, *114*, 163712.
[30] R. Mohanraman, R. Sankar, F. C. Chou, C. H. Lee, Y. Iizuka, I. P. Muthuselvam, Y. Y. Chen, *APL Mater.* **2014**, *2*, 096114.
[31] J. K. Lee, B. Ryu, S. Park, J. H. Son, J. Park, J. Jang, M. W. Oh, S. Park, *Acta Mater.* **2022**, *222*, 117443.
[32] M. Hong, Z. G. Chen, L. Yang, Z. M. Liao, Y. C. Zou, Y. H. Chen, S. Matsumura, J. Zou, *Adv. Energy Mater.* **2018**, *8*, 1702333.
[33] D. L. Medlin, J. D. Sugar, *Script. Mater.* **2010**, *62*, 379.
[34] J. H. Kim, H. Cho, S. Y. Back, J. H. Yun, H. S. Lee, J. Rhyee, *J. Alloy. Comp.* **2020**, *815*, 152649.
[35] J. H. Kim, S. Y. Back, J. H. Yun, H. S. Lee, J. Rhyee, *Materials* **2021**, *14*, 1564.
[36] C. Kittel, P. McEuen, *Introduction to Solid State Physics*, Wiley, New York **1996**.
[37] P. Sheng, B. Abeles, Y. Arie, *Phys. Rev. Lett.* **1973**, *31*, 44.
[38] D. Bilc, S. D. Mahanti, E. Quarez, K. F. Hsu, R. Pcionek, M. G. Kanatzidis, *Phys. Rev. Lett.* **2004**, *93*, 146403.
[39] D. Joung, S. I. Khondaker, *Phys. Rev. B* **2012**, *86*, 235423.
[40] N. F. Mott, *Adv. Phys.* **1967**, *16*, 49.
[41] K. G. Raj, P. A. Joy, *Phys. Chem. Chem. Phys.* **2015**, *17*, 16178.
[42] D. Das, K. Malik, A. K. Deb, V. A. Kulbachinskii, V. G. Kytin, S. Chatterjee, D. Das, S. Dhara, S. Bandyopadhyay, A. Banerjee, *Eur. Lett.* **2016**, *113*, 47004.
[43] N. F. Hinsche, B. Y. Yavorsky, I. Mertig, P. Zahn, *Phys. Rev. B* **2011**, *84*, 165214.

© 2023 The Authors. Advanced Functional Materials published by Wiley-VCH GmbH

16163028, 2024, 42, Downloaded from https://advanced.onlinelibrary.wiley.com/doi/10.1002/adfm.202404886 by Ewha Womans University Library, Wiley Online Library on [06/04/2025]. See the Terms and Conditions (https://onlinelibrary.wiley.com/terms-and-conditions) on Wiley Online Library for rules of use; OA articles are governed by the applicable Creative Commons License